Ju et al. *NPG Asia Materials* (2025)17:20
https://doi.org/10.1038/s41427-025-00602-x

NPG Asia Materials

ARTICLE Open Access

High-pressure phases of van der Waals Weyl semimetal transition metal ditellurides

Hwiin Ju[1], Siwon Oh[2], Heejung Kim[3], Duk Hyun Lee[4], Choongjae Won[5,6], Suyong Jung[4], Hyeonsik Cheong[2] and Jong Seok Lee[1]

Abstract

Previous high-pressure studies about WTe_2 have reported divergent critical pressures for structural and electronic phase transitions, obscuring a comprehensive understanding about the complex quantum phases. In this work, we precisely assign the structural phase evolutions and relevant electronic changes of type-II Weyl semimetals, WTe_2 and $MoTe_2$, using various optical methods. We confirm that the T_d to 1T′ structural phase transition occurs at about 2.5 GPa concomitantly with the previously reported decrease of magnetoresistance and emergence of superconductivity. Notably, electron-phonon coupling remains intact despite pressure-dependent variations in structural symmetry and atomic bond strengths, providing crucial insights into the origin of superconductivity in transition metal ditellurides. We also demonstrate an additional structural transition at about 10 GPa, possibly to a triclinic 1T″ structure, which has a significant influence on the electronic structure due to intra-layer distortion of atomic positions. Our findings on distinct evolutions of inter-layer and intra-layer structural parameters offer a generic understanding of the relationship between anisotropic bond strength in the van der Waals materials and pressure-dependent structural changes.

Introduction

The discovery of topological materials evoked a paradigm shift in classifying phases of matter, moving from Landau formalism, which relies on symmetry, to an additional consideration of topological order[1]. One recent observation concerns the massless Weyl-fermion. Among others, transition metal ditellurides have been extensively investigated as so-called type-II Weyl semimetals[2–4]. Numerous studies on this class of materials have revealed several exotic topological properties, including the intrinsic anomalous Hall effect[5–7] and large non-saturating magnetoresistance[8]. In particular, high-pressure investigations have been performed to improve the understanding of Weyl physics by modulating the crystalline structure and the electronic phases. By applying pressure to WTe_2, various resultant behaviors were demonstrated, such as a large reduction of magnetoresistance (MR)[9] and an emergence of superconductivity (SC)[10,11]. To discuss these electronic transitions from a structural perspective, several studies have employed X-ray diffraction[11,12] and Raman spectroscopy[11–13]. As summarized in Fig. 1a, however, reports investigating structural phase changes differ from each other in terms of the pressure values of the phase transition. Furthermore, the pressure values of the structural transitions deviate from those of other electrical[14] and optical[15] measurements, which can obscure understanding of the underlying mechanisms of electronic and topological phase evolutions. Therefore, defining accurate pressure-induced phases of transition metal ditellurides is urgently required to establish a rigorous connection between structural phases and other physical phenomena.

In this study, we precisely trace the pressure-dependent evolutions of the crystalline structure and electronic states of transition metal ditellurides (WTe_2 and $MoTe_2$) using optical techniques, including low-frequency Raman spectroscopy, optical pump-probe (OPOP), and optical second-harmonic generation (SHG) methods. These optical measurements are highly sensitive to crystalline symmetry, enabling the precise determination of pressure-dependent structural phases. We undoubtedly

Correspondence: Jong Seok Lee (jsl@gist.ac.kr)
[1]Department of Physics and Photon Science, Gwangju Institute of Science and Technology (GIST), Gwangju, Republic of Korea
[2]Department of Physics and Center for Nano Materials, Sogang University, Seoul, Korea
Full list of author information is available at the end of the article
These authors contributed equally: Hwiin Ju, Siwon Oh

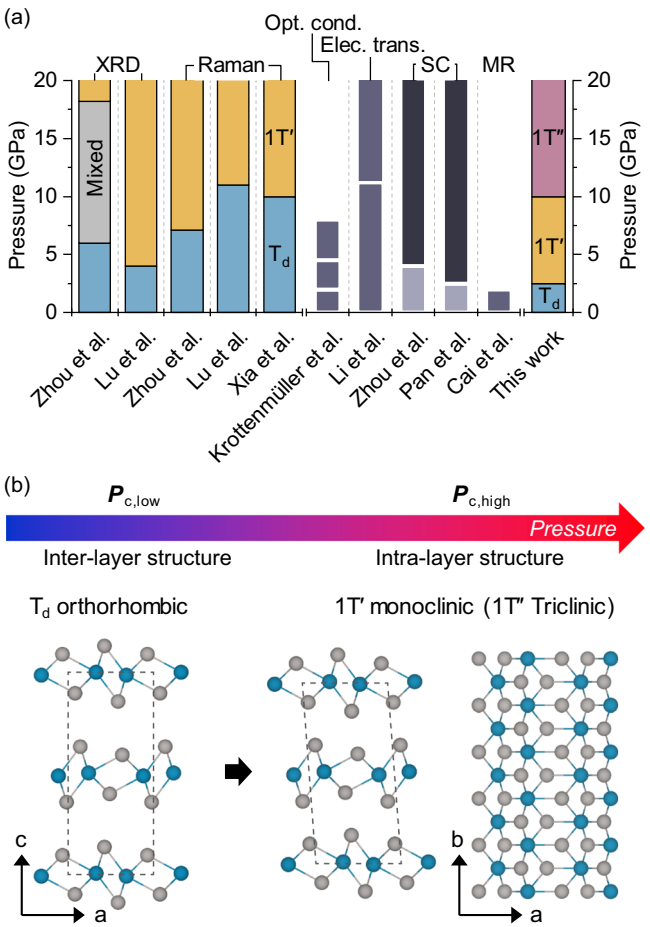

Fig. 1 Pressure-dependent changes in the structural, optical, and electronic properties of WTe_2. a Previous studies defining phases of WTe_2 at high pressures[9–15]. Structural phases are shown with blue, yellow, and red bars for T_d, 1T′, and 1T″ phases, respectively. The columns in the middle display pressure values for anomalies in optical conductivity (Opt. cond.), electric transport (Elec. trans.), superconductivity (SC), indicated with breaks. In the case of the magnetoresistance (MR), a measurement was done only in a low-pressure region below about 2.4 GPa. Pressure ranges exhibiting superconducting (non-superconducting) states are colored with darker (brighter) gray color. The structural phase evolution revealed by this work is shown on the right. **b** Structural phases of WTe_2 at high pressures as verified in this work. Side views and top view of atomic structures of T_d and 1T′ phase are shown for comparison. The 1T″ phase has a similar crystalline structure to 1T′, showing a difference in the atomic network at the inside of the layer (Supplementary Information S8).

demonstrate that WTe_2 undergoes a structural phase transition from the orthorhombic T_d phase to the monoclinic 1T′ phase at about 2.5 GPa. Furthermore, we find another phase transition at about 10 GPa, possibly into the triclinic 1T″ phase. Since the pressure values of these structural phase transitions are in excellent agreement with those of previous electric and optical properties, including superconductivity[9,10,14,15], these findings will elaborate the understanding of topological and electronic phase evolutions linked with structural phases in transition metal ditellurides.

Results and Discussion

We first examine the pressure-dependent structural changes based on the Raman scattering results. Figure 2a shows the Raman spectra of WTe_2, which exhibit a large variation upon increasing pressure. At ambient pressure, six peaks are observed in a parallel polarization configuration (*xx*), consistent with previous results[16,17]. Irreducible representation of optical phonons at the Γ point is $\Gamma = 11A_1 + 6A_2 + 5B_1 + 11B_2$[16]. Although these modes are Raman-active, only A_1 and A_2 modes are observed in our backscattering geometry. Raman peaks in ambient pressure are maintained until 2.0 GPa, and abrupt changes occur at about 2.5 GPa. Here, the peak of the A_1^1 mode and two peaks of the A_1^{4-6} modes are lost, while a weak peak appears at 95 cm^{-1}. The loss of phonon peaks is attributed to the change of Raman-active A_1 modes in the T_d structure into infrared-active B_u modes in the 1T′ structure[16,18–20]. The mode appearing at 95 cm^{-1}

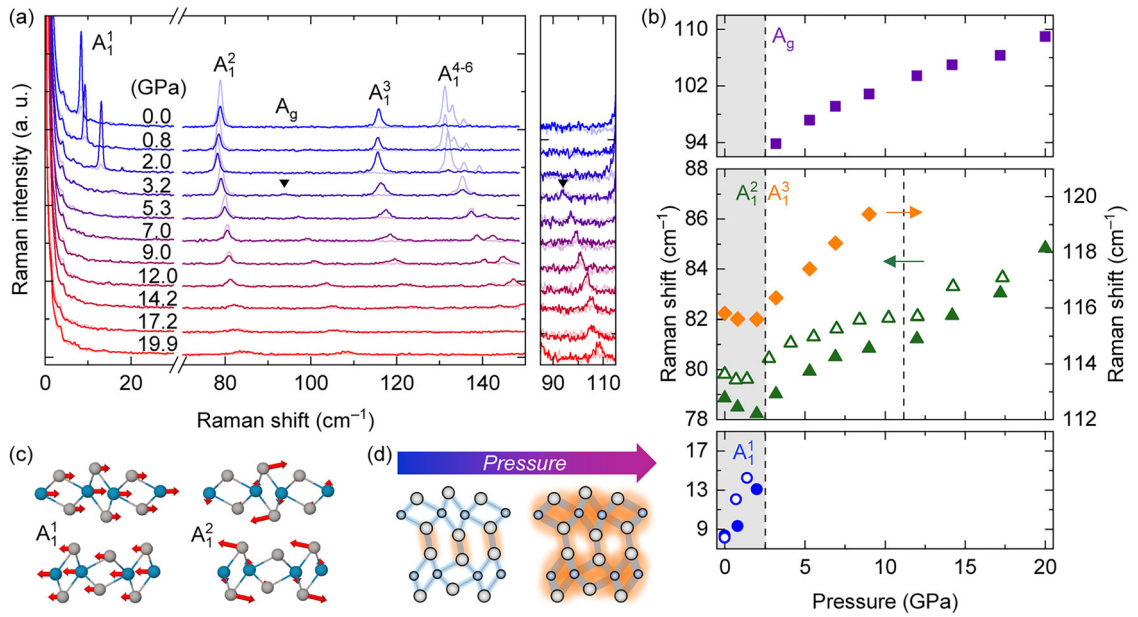

Fig. 2 Raman spectroscopy results of WTe_2 depending on the hydrostatic pressure applied. a Pressure-dependent polarized Raman spectra of WTe_2 at room temperature. Dark (bright) lines correspond to results obtained in the parallel (cross) polarization configuration. The A_g Raman mode observed in the 1T′ phase is indicated with black triangles. **b** Pressure-dependent peak positions of selected Raman modes. Phonon peaks achieved from Raman spectroscopy (optical pump-probe) are displayed with closed (open) symbols. **c** Atomic motions of A_1^1 and A_1^2 Raman modes. **d** Schematic of the pressure-dependent bonding strength changes. The red (blue) shadow indicates an increase (decrease) in the bond strength.

corresponds to the A_g mode in the 1T′ structure[16,18–20]. Although previous studies claimed that the T_d to 1T′ structural transition occurs at pressures ranging from 4 GPa to 10 GPa[11–13], our Raman scattering results (covering a wide spectral range, down to 5 cm^{-1}) conclude that it occurs at 2.5 GPa. The complete disappearance of the A_1^1 mode suggests that the entire area has undergone a transition.

We confirm the pressure-induced structural phase transition at 2.5 GPa based on an independently performed optical pump-probe experiment. Figure 3a shows the optical pump-induced transient reflectivity obtained as a function of a pump-probe time delay at various pressures. The transient reflectivity at ambient pressure exhibits a rapid rise followed by a gradual relaxation. Superimposed onto this behavior is a well-defined oscillation, which is attributed to coherently oscillating phonons[21,22]. Whereas acoustic phonons often give rise to the oscillatory response after the photo-excitation[23–25], we attribute our observation for the bulk-like samples to the contribution of the optical phonon. Fourier transform of the oscillation part is plotted in Fig. 3b. At ambient pressure, three distinct peaks are observed at 8 cm^{-1}, 80 cm^{-1}, and 132 cm^{-1}, and are assigned to A_1^1, A_1^2, and one among A_1^{4-6} modes, respectively, according to their frequencies[16,17]. Peak frequencies obtained from Raman spectroscopy and OPOP have discrepancies less than 1 cm^{-1}, depending on the calibration of Raman spectrum. As the pressure increases, the transient reflectivity shows a significant change. Interestingly, the long-period oscillation corresponding to the A_1^1 mode disappears at 2.5 GPa, in agreement with the Raman scattering results shown in Fig. 2. The pressure dependence of the A_1^2 mode is also consistent with the Raman measurements. These results suggest the reliability of our observation and reconfirm the presence of T_d–1T′ phase transition at 2.5 GPa for WTe_2. A similar structural transition with the pressure application can be reproduced based on the density functional theory (DFT) calculation (Supplementary Information S2).

By investigating the details of pressure-dependent phonon modes, we obtain important insights about the microscopic structural evolution across 2.5 GPa. Pressure-dependent frequency changes of four representative modes are plotted in Fig. 2b. Upon a pressure increase up to 2 GPa, the A_1^1 mode is significantly hardened with its frequency increased by about 60%. Considering that the A_1^1 mode is the inter-layer shear vibration mode[16], its hardening is understood as a large reduction in inter-layer spacing under the application of hydrostatic pressure[11,26,27]. On the other hand, the other phonons involved with the intra-layer atomic motions, namely A_1^2 and A_1^3 modes, are softened with an increase in pressure. As pressure application typically shortens inter-atomic distance and enhances atomic bond strength, it is rare to see such phonon softenings of intra-layer modes and

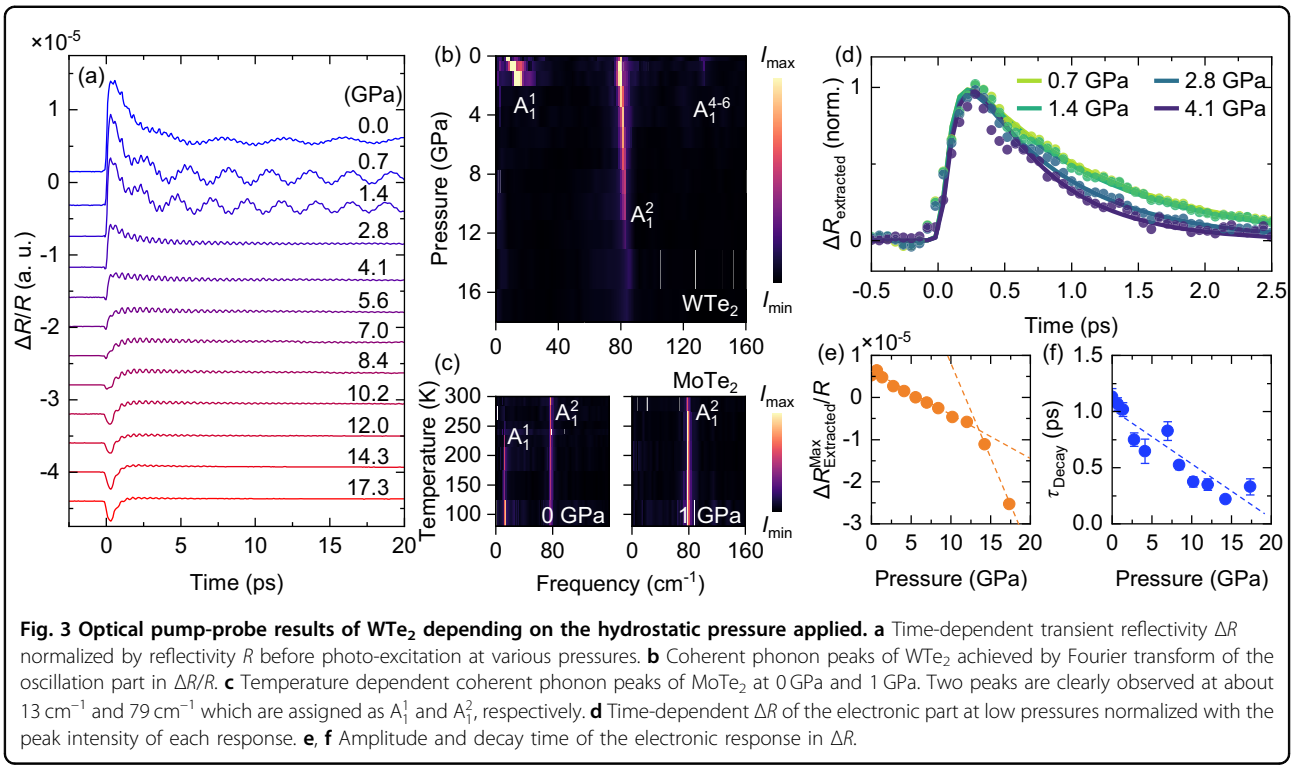

Fig. 3 Optical pump-probe results of WTe_2 depending on the hydrostatic pressure applied. a Time-dependent transient reflectivity ΔR normalized by reflectivity R before photo-excitation at various pressures. **b** Coherent phonon peaks of WTe_2 achieved by Fourier transform of the oscillation part in $\Delta R/R$. **c** Temperature dependent coherent phonon peaks of $MoTe_2$ at 0 GPa and 1 GPa. Two peaks are clearly observed at about 13 cm^{-1} and 79 cm^{-1} which are assigned as A_1^1 and A_1^2, respectively. **d** Time-dependent ΔR of the electronic part at low pressures normalized with the peak intensity of each response. **e**, **f** Amplitude and decay time of the electronic response in ΔR.

opposite pressure-dependent trends of inter-layer and intra-layer modes. Whereas the T_d to 1T′ structure transition occurs mainly via inter-layer sliding (Supplementary Information S2), this intra-layer phonon softening with application of pressure indicates that intra-layer phonons may also contribute to the structural phase transition. Upon phase transition, frequencies of A_1^2 and A_1^3 modes show sudden increases to values larger than those at ambient pressure. After the phase transition, i.e., above 2.5 GPa, they exhibit conventional pressure-dependent increases.

It should be noted that there have been previous works reporting the emergence of an SC ground state in WTe_2 at about 2.5 GPa[10,11]. Concurrently, a large reduction of MR is observed at the same pressure[9,10], indicating the breaking of balance between the electron and hole pockets in the Weyl band[8,28]. Pressure-induced symmetry change and destabilization of the Weyl state are expected at this pressure. However, earlier structural investigations reported the structural transition at much higher pressures[11–13]; hence, the connection between the structural change and the pressure-induced superconducting ground state has been unclear. In this work, we confirm that the structural transition from T_d to 1T′ occurs at 2.5 GPa for WTe_2. Thus, it is now clear that both structural and superconducting transitions occur at a similar pressure for WTe_2, and it is worthwhile to consider their connection in more detail.

Interestingly, similar pressure-dependent phase evolutions are observed in $MoTe_2$, which is another representative transition metal ditelluride. From the temperature-dependent transient reflectivity results obtained after photo-excitation, we found that T_d to 1T′ structural transition temperature rapidly decreases from 250 K to under 80 K below the 1 GPa pressure application (Fig. 3c). This may indicate that the low-temperature (~5 K) structural phase of $MoTe_2$ changes from T_d to 1T′ at about 1 GPa, where the superconducting transition temperature shows a rapid increase[29]. These behaviors are analogous to those observed in WTe_2. Interestingly, similar phase evolutions can be found in $MoTe_2$ with thickness variation. Recently, Rhodes et al. reported that the superconducting transition temperature of $MoTe_2$ increases with thinner flakes[30]. Importantly, when the $MoTe_2$ layer becomes thinner, the translational symmetry is broken, the 1T′ structure is stabilized, and the frequency of the A_1^2 Raman mode increases[19]. These behaviors are the same as those observed for WTe_2 and $MoTe_2$ under pressure application. Such pressure- and thickness-dependent observations elaborate the discussion about interconnection among the structural transition, anomalous behavior of intra-/inter-layer bond strength, and superconductivity in transition metal ditellurides. Furthermore, as the structural transition from T_d to 1T′ should be accompanied by a topological phase transition from the Weyl semimetal state to the non-Weyl state, it

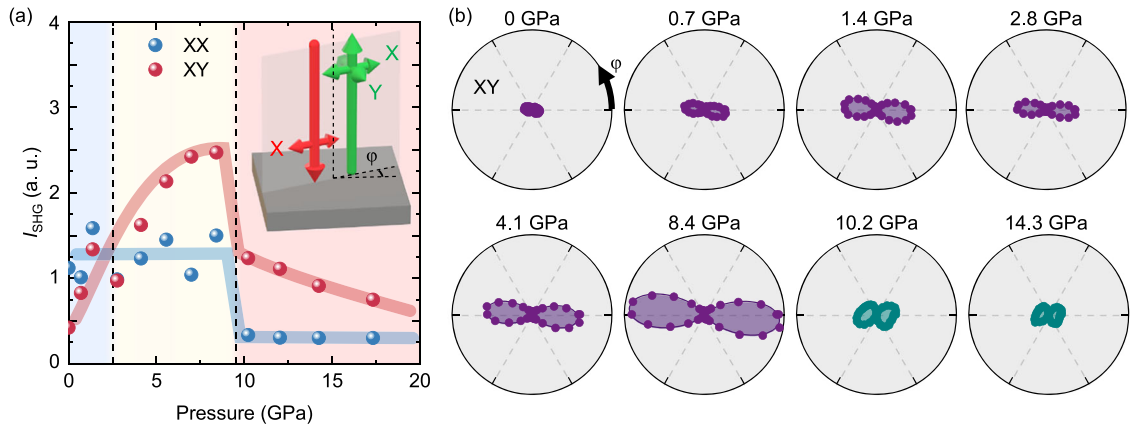

Fig. 4 Second-harmonic generation (SHG) results depending on the hydrostatic pressure applied. a Pressure-dependent SHG intensity. Results obtained in parallel (XX) and cross (XY) polarization configurations are displayed with blue and red circles, respectively. The inset shows an experimental scheme of the SHG measurement. **b** Azimuth-dependent SHG patterns obtained with a variation of polarization angle (φ) in the XY polarization configuration. Fitting results are indicated with filled patterns.

would be intriguing to examine the correlation between the Weyl state and the superconducting phase[31].

In addition to the structural changes, we examine evolutions of the electronic state and the electron-phonon coupling with the pressure increase based on the optical pump-probe experimental results. As photo-excitation changes the occupation of electronic states, the rise and relaxation of the transient reflectivity provide important information about the electronic states[32,33]. As shown in Fig. 3a, the OPOP signal exhibits large pressure-dependent variations in its rise and relaxation. As the pressure increases, the amplitude of the electronic part (Supplementary Information S4) monotonically decreases, crosses a zero level, and becomes negative (Fig. 3e). It should be noted that such pressure-dependent variation is quite monotonic with no discernible anomaly until 10 GPa. (The anomaly is discussed later.) Such continuous variation of the OPOP response with an increase in pressure is unexpected considering that the crystalline structural symmetry undergoes abrupt changes around 2.5 GPa. Furthermore, the relaxation of the OPOP signal does not involve any noticeable anomaly around 2.5 GPa. Decay time, obtained from exponential fitting, decreases continuously with the pressure increase, as shown in Fig. 3f. In the two-temperature model that considers the energy exchange between electron and phonon sub-systems, the decay time of the transient reflectivity is $\tau_e = C_e/G_{ep}$, where C_e is electron heat capacity and G_{ep} is electron-phonon coupling strength[34]. Although there are no specific results about the pressure-dependent change of C_e, a previous study reporting a small variation in the electron density across 2.5 GPa suggests that C_e does not experience a meaningful change upon the structural transition[14]. From this expectation of C_e and the result of τ_e, we conjecture that the electron-phonon coupling strength remains almost unchanged across 2.5 GPa, where the superconducting ground state becomes stabilized.

We now discuss anomaly of pressure-induced phase in WTe_2 at about 10 GPa. At this pressure, the A_1^3 phonon mode almost disappears, and the A_1^2 mode shows an additional frequency shift (Fig. 2). Also, the amplitude of the electronic part in the transient reflectivity shows a clear change in its pressure-dependent slope near 10 GPa (Fig. 3). Previous studies about high-pressure structural phase utilizing Raman and XRD measurements, and those about electrical transport also reported anomalies around 10 GPa, regardless of pressure medium, although these were mislabeled as the T_d–1T′ structural phase transition[11–13]. We attribute the large deviation in pressure-dependent structural changes in several previous reports partly to an ignorance of the second structural transition, which is clearly demonstrated in this work.

To have a better understanding of structural changes, we performed SHG measurement, which is highly sensitive to the structural symmetry of materials. Figure 4b shows the azimuth-dependent SHG signal of WTe_2 with the orthogonal (XY) polarization configuration for the fundamental and second-harmonic waves. Note that the SHG intensity is quadratically proportional to the fundamental light intensity (not shown), confirming the second harmonic generation from the WTe_2 sample. While the SHG intensity slightly changes at the T_d–1T′ phase boundary (~2.5 GPa), a two-fold anisotropy pattern persists until 8.4 GPa. The observed anisotropy patterns are fitted well with point group *m* due to the symmetry of the surface of WTe_2 (Fig. S8). Around 10 GPa, we observe an abrupt change in the SHG responses; together with the intensity reduction, the two-fold SHG pattern becomes largely distorted. This anisotropy pattern cannot be fitted with symmetry *m*, but it can be fitted either by

considering the multi-domain or by removing the mirror symmetry. Between these two scenarios, domain formation cannot account for the disappearance or appearance of Raman peak (A_1^3), and it cannot explain the significant electron density change observed by Li et al.[14], either. Thus the more plausible scenario is to consider the structure with triclinic symmetry 1, which is achieved by removing a mirror symmetry operation from point group *m* (Fig. S9). Among transition metal dichalcogenides, ReS_2 has a triclinic structure 1T″ with bulk and surface point groups $\bar{1}$ and 1, respectively. A transition to the ReS_2-like structure should be accompanied by a distortion of the intra-layer atomic positions[35,36] (Fig. S10). This is consistent with the large frequency shift of the A_1^2 mode, mainly due to intra-layer structural changes. Thus, we suggest a structural phase transition around 10 GPa from the 1T′ phase possibly to the triclinic 1T″ phase whereas broadening of Raman peaks may indicate a phase mixture above 10 GPa.

Although the transition from 1T′ to 1T″ arises due to breaking of a single additional mirror symmetry, it should also be accompanied by a change in the atomic network within the van der Waals (vdW) layer; this can lead to corresponding changes in the electronic properties. As mentioned previously, we find large changes in the OPOP amplitude (Fig. 3e) and SHG signal (Fig. 4a). Also, Li et al. reported a dramatic change in the electronic transport properties of WTe_2 around 10 GPa[14]. These properties exhibit much smaller changes around 2.5 GPa where the structural change is caused mainly by inter-layer sliding. These results suggest that the structural changes of the intra-layer atomic network occur at a much higher pressure than those of the inter-layer network (Fig. 1b), and this can have a significant influence on the electronic structure owing to the strong intra-layer covalent bonds in vdW materials. Although the transition to the 1T″ structure greatly modifies electronic characteristics, it does not break the inversion symmetry, which enables WTe_2 to persist in the topologically trivial non-Weyl state after the transition.

Conclusions

In conclusion, we successfully assigned the structural phases of WTe_2 and $MoTe_2$ with a variation of hydrostatic pressure employing various optical methods, which include ultralow frequency Raman spectroscopy and optical second-harmonic generation measurement, and also the density functional theory calculations. We showed that the T_d to 1T′ structural phase transition occurs at about 2.5 GPa induced by inter-layer sliding. We also demonstrated an additional structural transition around 10 GPa with a possible transition to the triclinic 1T″ phase, which should be involved with intra-layer distortion of atomic position. These results provide a straightforward intuition of anisotropic bond strength between inter-layer and intra-layer in this van der Waals materials, and accordingly give an approximate range of the transition pressure for inter-layer or intra-layer structural phase transitions. Our result reveals that T_d to 1T′ transition occurs concomitantly with the previously reported decrease in magnetoresistance and the emergence of the superconductivity[9–11]. Also, 1T′ to 1T″ transition is accompanied by a large change in electronic properties[14]. Therefore, the results presented in this work provide important hints that can increase understanding of the pressure-induced topological phase transition and the emergence of superconductivity in transition metal ditellurides. Also, this work can be an important guide in exploiting transition metal ditellurides in spintronic and electronic devices by modulating selectively the inter-layer and intra-layer structural networks with external stimuli.

Methods

Raman spectroscopy

Raman measurements were carried out using the 633 nm (1.96 eV) line of a He-Ne laser. The laser beam was focused onto the sample with a long-working-distance objective lens (0.4 NA). The scattered beam was collected with the same objective lens in the back-scattering geometry. A HORIBA iHR550 spectrometer with a liquid-nitrogen-cooled, back-illuminated CCD (Horiba) was used. Volume holographic filters (Opti-Grate) were used to eliminate Rayleigh-scattered light, enabling ultralow-frequency Raman measurement. The polarization states of incident light and scattered light were determined with polarizers and half-wave plates.

Optical pump-probe measurement

Pump-probe measurements were performed using laser pulses with a 780 nm wavelength and 80 fs pulse width generated from a Ti:sapphire laser (Vitara-T). The pump and probe light were separated by a beam splitter and were partitioned with optical filters. The pump light was modulated at 100 kHz using a photoelastic modulator and focused onto the sample with a ×20 objective lens in the normal incidence geometry. The probe light passed through the same objective lens, and the reflected light was collected with a Si photodiode. A lock-in amplifier selected the oscillating part (100 kHz) of the probe signal that had the same modulation frequency as the pump light. The pump-induced changes in the probe signal were measured with a time step of 60 fs, extending up to a pump-probe time delay of 27 ps.

Optical second-harmonic generation measurement

Light with an 800 nm wavelength and 80 MHz repetition rate was generated from the Ti:sapphire laser (Vitara-T)

and focused on to the sample with an ×20 objective lens in the normal incidence geometry. Second-harmonic light (400 nm) was generated from the sample, reflected back, and collimated with the same objective lens. Collimated second-harmonic light was guided with a dichroic mirror and collected with a photomultiplier tube (PMT). Optical filters were used to block other light (except 400 nm light). A Glan-Thompson polarizer and half-wave plate were used to define the polarization of incident light. The Glan-Taylor polarizer was placed in front of the PMT to select second-harmonic light in a specific polarization direction. Azimuth-dependent SHG anisotropy patterns were measured by simultaneously rotating the input and output laser polarizations, which were set to be parallel (XX) or perpendicular (XY) to each other.

Sample preparation and high-pressure measurement

Single-crystalline samples (synthesized or provided by HQ graphene and 2D semiconductors) were exfoliated and transferred directly onto the diamond of the pressure cell using a PDMS film (gel-pak). Note that samples are 50–100 nm thick, and hence they reflect bulk properties. We repeated the pressure-dependent experiments on several samples with no intentional control of their thickness, and found consistent results for all the samples investigated. High-pressure experiments were performed using a diamond anvil cell (Almax easyLab). SS304L stainless steel gaskets were pre-indented to a thickness of 60 μm. A 150-μm-diameter hole was drilled at its center to form the sample chamber. Ruby powder was placed inside the gasket, and photoluminescence of the ruby powder was achieved using a 514-nm argon laser for pressure calibration. A 4:1 methanol:ethanol mixture was used as a pressure medium. Low-temperature measurement was performed with an Oxford cryostat and custom-built shield.

Acknowledgements
The work at GIST was supported by the National Research Foundation of Korea (NRF) grant funded by the Korean government (MSIT) (No. RS-2022-NR070254, No. RS-2022-NR068223). The work at Sogang University was supported by National Research Foundation of Korea (NRF) grant funded by the Korean government (MSIT) (RS-2024-00450714) and the G-LAMP project (RS-2024-00441954) funded by the Ministry of Education. The work of H.K. was supported by the National Research Foundation of Korea (NRF) grant funded by the Korean government (MSIT) (Grant No. 2021R1C1C2011276). D.H.L. and S.J. acknowledge the support from the Basic Science Research Program through the National Research Foundation of Korea (NRF) under grant no. NRF-2022R1A2C2008140. The work of C.W. was supported by the National Research Foundation of Korea funded by the Ministry of Science and ICT (grant No. RS-2022-NR068223).

Author details
[1]Department of Physics and Photon Science, Gwangju Institute of Science and Technology (GIST), Gwangju, Republic of Korea. [2]Department of Physics and Center for Nano Materials, Sogang University, Seoul, Korea. [3]Center for Theoretical Physics, Seoul National University, Seoul, Republic of Korea. [4]Korea Research Institute of Standards and Science, Daejeon, Republic of Korea. [5]Max Planck POSTECH Center for Complex Phase Materials, Department of Physics, Pohang University of Science and Technology, Pohang, Korea. [6]Laboratory for Pohang Emergent Materials, Department of Physics, Pohang University of Science and Technology, Pohang, Korea

Author contributions
H.J. and J.S.L. conceived the idea and designed the experiments. H.J. prepared a high-pressure experiment using diamond anvil cell and performed the SHG and OPOP experiments under the supervision of J.S.L. S.O. conducted the Raman experiment under the supervision of H.C. H.K. performed the DFT calculations. D.H.L. and S.J. prepared the samples in the diamond anvil cell. C.W. synthesized the $MoTe_2$ single crystals. H.J. and J.S.L. drafted the manuscript initially and revised it based on input and feedback from all the authors. J.S.L. supervised and directed all aspects of the project.

Data availability
The data that support the findings of this work are available from the corresponding author upon reasonable request.

Competing interests
The authors declare no competing interests.

Ethics approval and consent to participate
This study does not require ethics approval or consent to participate, as the research did not involve live vertebrates (animals), human participants, or any identifiable images.

Supplementary information The online version contains supplementary material available at https://doi.org/10.1038/s41427-025-00602-x.

Received: 3 October 2024 Accepted: 3 April 2025
Published online: 30 April 2025

References
1. Hasan, M. Z. & Kane, C. L. Colloquium: Topological insulators. *Rev. Mod. Phys.* **82**, 3045–3067 (2010).
2. Soluyanov, A. A. et al. Type-II Weyl semimetals. *Nature* **527**, 495–498 (2015).
3. Deng, K. et al. Experimental observation of topological Fermi arcs in type-II Weyl semimetal $MoTe_2$. *Nat. Phys.* **12**, 1105–1110 (2016).
4. Li, P. et al. Evidence for topological type-II Weyl semimetal WTe_2. *Nat. Commun.* **8**, 2150 (2017).
5. Ma, Q. et al. Observation of the nonlinear Hall effect under time-reversal-symmetric conditions. *Nature* **565**, 337–342 (2019).
6. Kang, K., Li, T., Sohn, E., Shan, J. & Mak, K. F. Nonlinear anomalous Hall effect in few-layer WTe_2. *Nat. Mater.* **18**, 324–328 (2019).
7. Tiwari, A. et al. Giant c-axis nonlinear anomalous Hall effect in T_d-$MoTe_2$ and WTe_2. *Nat. Commun.* **12**, 2049 (2021).
8. Ali, M. N. et al. Large, non-saturating magnetoresistance in WTe_2. *Nature* **514**, 205–208 (2014).
9. Cai, P. L. et al. Drastic pressure effect on the extremely large magnetoresistance in WTe_2: Quantum oscillation study. *Phys. Rev. Lett.* **115**, 057202 (2015).
10. Pan, X.-C. et al. Pressure-driven dome-shaped superconductivity and electronic structural evolution in tungsten ditelluride. *Nat. Commun.* **6**, 7805 (2015).
11. Zhou, Y. et al. Pressure-induced T_d to 1T′ structural phase transition in WTe_2. *AIP Adv.* **6**, 075008 (2016).
12. Lu, P. et al. Origin of superconductivity in the Weyl semimetal WTe_2 under pressure. *Phys. Rev. B* **94**, 224512 (2016).
13. Xia, J. et al. Pressure-induced phase transition in Weyl Semimetallic WTe_2. *Small* **13**, 1701887 (2017).
14. Li, Y. et al. Electrical transport properties of Weyl semimetal WTe_2 under high pressure. *J. Mater. Sci.* **55**, 14873–14882 (2020).
15. Krottenmüller, M., Ebad-Allah, J., Süss, V., Felser, C. & Kuntscher, C. A. Optical conductivity of the type-II Weyl semimetal WTe_2 under pressure. *Phys. Rev. B* **102**, 075122 (2020).

16. Ma, X. et al. Raman scattering in the transition-metal dichalcogenides of 1T′-$MoTe_2$, T_d-$MoTe_2$, and T_d-WTe_2. *Phys. Rev. B* **94**, 214105 (2016).
17. Jiang, Y. C., Gao, J. & Wang, L. Raman fingerprint for semi-metal WTe_2 evolving from bulk to monolayer. *Sci. Rep.* **6**, 19624 (2016).
18. Chen, S.-Y., Goldstein, T., Venkataraman, D., Ramasubramaniam, A. & Yan, J. Activation of New Raman modes by inversion symmetry breaking in Type II Weyl semimetal candidate T′-$MoTe_2$. *Nano Lett.* **16**, 5852–5860 (2016).
19. Cheon, Y., Lim, S. Y., Kim, K. & Cheong, H. Structural phase transition and interlayer coupling in few-layer 1T′ and T_d $MoTe_2$. *ACS Nano* **15**, 2962–2970 (2021).
20. Zhang, K. et al. Raman signatures of inversion symmetry breaking and structural phase transition in type-II Weyl semimetal $MoTe_2$. *Nat. Commun.* **7**, 13552 (2016).
21. Zeiger, H. J. et al. Theory for displacive excitation of coherent phonons. *Phys. Rev. B* **45**, 768–778 (1992).
22. Cho, G. C., Kütt, W. & Kurz, H. Subpicosecond time-resolved coherent-phonon oscillations in GaAs. *Phys. Rev. Lett.* **65**, 764–766 (1990).
23. Thomsen, C. et al. Coherent Phonon generation and detection by Picosecond light pulses. *Phys. Rev. Lett.* **53**, 989–992 (1984).
24. Thomsen, C., Grahn, H. T., Maris, H. J. & Tauc, J. Surface generation and detection of phonons by picosecond light pulses. *Phys. Rev. B* **34**, 4129–4138 (1986).
25. Jang, H. et al. Transient SHG imaging on ultrafast carrier dynamics of MoS_2 nanosheets. *Adv. Mater.* **30**, 1705190 (2018).
26. Pei, S., Wang, Z. & Xia, J. High pressure studies of 2D materials and heterostructures: A review. *Mater. Des.* **213**, 110363 (2022).
27. Zhang, L. et al. 2D Materials and Heterostructures at Extreme Pressure. *Adv. Sci.* **7**, 2002697 (2020).
28. Shekhar, C. et al. Extremely large magnetoresistance and ultrahigh mobility in the topological Weyl semimetal candidate NbP. *Nat. Phys.* **11**, 645–649 (2015).
29. Qi, Y. et al. Superconductivity in Weyl semimetal candidate $MoTe_2$. *Nat. Commun.* **7**, 11038 (2016).
30. Rhodes, D. A. et al. Enhanced superconductivity in monolayer T_d-$MoTe_2$. *Nano Lett.* **21**, 2505–2511 (2021).
31. Li, Y. & Xu, Z.-A. Exploring topological superconductivity in topological materials. *Adv. Quantum Technol.* **2**, 1800112 (2019).
32. Sun, C. K., Vallée, F., Acioli, L. H., Ippen, E. P. & Fujimoto, J. G. Femtosecond-tunable measurement of electron thermalization in gold. *Phys. Rev. B* **50**, 15337–15348 (1994).
33. Choi, I. H. et al. Giant enhancement of electron–phonon coupling in dimensionality-controlled $SrRuO_3$ heterostructures. *Adv. Sci.* **10**, 2300012 (2023).
34. Qiu, T. Q. & Tien, C. L. Size effects on nonequilibrium laser heating of metal films. *J. Heat. Transf.* **115**, 842–847 (1993).
35. Murray, H. H., Kelty, S. P., Chianelli, R. R. & Day, C. S. Structure of Rhenium disulfide. *Inorg. Chem.* **33**, 4418–4420 (1994).
36. Xiao, Y., Zhou, M., Liu, J., Xu, J. & Fu, L. Phase engineering of two-dimensional transition metal dichalcogenides. *Sci. China Mater.* **62**, 759–775 (2019).